# Sustainable thermoelectric materials fabricated by using $Cu_2Sn_{1-x}Zn_xS_3$ nanoparticles as building blocks

Wei Zhou,[1] Chiko Shijimaya,[1] Mari Takahashi,[1] Masanobu Miyata,[1] Derrick Mott,[1] Mikio Koyano,[1] Michihiro Ohta,[2] Takeo Akatsuka,[3] Hironobu Ono,[3] and Shinya Maenosono[1,a)]

[1]*School of Materials Science, Japan Advanced Institute of Science and Technology, 1-1 Asahidai, Nomi, Ishikawa 923-1292, Japan*
[2]*Research Institute for Energy Conservation, National Institute of Advanced Industrial Science and Technology (AIST), Tsukuba, Ibaraki 308-8568, Japan*
[3]*Research Center, Nippon Shokubai Co., Ltd., Himeji, Hyogo 671-1292, Japan*

(Received 17 October 2017; accepted 13 December 2017; published online 28 December 2017)

Uniform $Cu_2Sn_{1-x}Zn_xS_3$ ($x = 0$–0.2) nanoparticles (NPs) with a characteristic size of about 40 nm were chemically synthesized. The primary crystal phase of the NPs was wurtzite (WZ) with a mean crystalline size of about 20 nm. The NPs were sintered to form nanostructured pellets with different compositions preserving the composition and grain size of the original NPs by the pulse electric current sintering technique. The pellets had a zinc blende (ZB) structure with a residual WZ phase, and the mean crystalline size was found to remain virtually unchanged for all pellets. Among all samples, the pellets of $Cu_2Sn_{0.95}Zn_{0.05}S_3$ and $Cu_2Sn_{0.85}Zn_{0.15}S_3$ exhibited the highest $ZT$ value (0.37 at 670 K) which is 10 times higher than that of a non-nanostructured $Cu_2SnS_3$ bulk crystal thanks to effective phonon scattering by nanograins, the phase-pure ZB crystal structure, and the increase in hole carrier density by Zn doping.  https://doi.org/10.1063/1.5009594

Copper sulfide thermoelectric materials have recently attracted much attention due to their relatively high $ZT$ value along with the earth-abundant nature and low toxicity of their constituent elements. In 2011, it was reported that digenite ($Cu_{1.8}S$) with a second djurleite ($Cu_{1.96}S$) phase exhibited $ZT = 0.5$ at 673 K.[1] In 2013, Suekuni and co-workers found that $Cu_{10.5}Ni_{1.5}Sb_4S_{13}$ tetrahedrite exhibited $ZT = 0.7$ at 665 K.[2] Shortly thereafter, Suekuni and co-workers reported that $Cu_{26}V_2Ge_6S_{32}$ colusite had a $ZT$ value of 0.73 at 663 K.[3] At nearly the same time, several copper sulfide thermoelectric materials with a $ZT$ value exceeding 1, such as $Cu_{11}MnSb_4S_{13}$ tetrahedrite ($ZT = 1.13$ at 575 K),[4] $Cu_{10.5}Ni_{1.0}Zn_{0.5}Sb_4S_{13}$ tetrahedrite ($ZT = 1.03$ at 575 K),[5] and $Cu_{26}Ta_2Sn_{5.5}S_{32}$ colusite ($ZT \sim 1$ at 670 K),[6] had been reported from different groups. With this global trend of development of copper sulfide-based sustainable thermoelectric materials, researchers have revived interest in $Cu_2SnS_3$ (CTS) which had been well known as a solar cell material. Recently, Shen *et al.* have reported that Zn-doped CTS ($Cu_2Sn_{0.9}Zn_{0.1}S_3$) exhibited $ZT = 0.58$ at 723 K.[7] Tan *et al.* have also reported that In-doped CTS ($Cu_2Sn_{0.9}In_{0.1}S_3$) exhibited $ZT = 0.56$ at 773 K.[8] Zhao *et al.* have reported that Co-doped CTS ($Cu_2Sn_{0.8}Co_{0.2}S_3$) exhibited $ZT = 0.85$ at 723 K.[9]

On the other hand, multi-scale structuring has been regarded as one of the promising approaches to enhance the $ZT$ value of a thermoelectric material by enhancing phonon scattering with maintaining good carrier transport properties. For example, Kanatzidis *et al.* fabricated a PbTe-SrTe thermoelectric material with a hierarchically organized multi-scale defect structure (panoscopic structure), i.e., atomic defects, nano-endotaxial structures and mesoscale grain boundaries, which exhibited $ZT = 2.2$ at 915 K.[10] To fabricate panoscopic thermoelectric materials, the bottom-up preparation approach in which chemically synthesized nanoparticles (NPs) are used as building blocks for making the panoscopic materials is promising. This enables us to easily create exotic structures never before possible by introducing atomic defects in NPs (including impurities) during the synthesis, controlling size and shape of the NPs, blending two or more different types of NPs for making a bulk material, and controlling mesoscale defect structures by taking advantage of the pulse electric current sintering (PECS) technique.

With this in mind, in this study, we chemically synthesized uniform hole-doped CTS ($Cu_2Sn_{1-x}Zn_xS_3$) NPs and fabricated sustainable thermoelectric materials by sintering the NPs into dense bulk materials by PECS. Then, the structure-composition-property relationships in the $Cu_2Sn_{1-x}Zn_xS_3$ thermoelectric materials were analyzed. To avoid misunderstanding, we emphasize the differences between $Cu_2ZnSnS_4$ (CZTS) and $Cu_2Sn_{1-x}Zn_xS_3$ (Zn-doped CTS). CZTS has also been well known since early times as a promising quaternary p-type semiconductor material for solar energy conversion and photocatalysts with a bandgap of 1.45 – 1.50 eV. In addition, a nanostructured bulk thermoelectric material has been fabricated by using chemically synthesized CZTS NPs.[11] However, the $ZT$ value of the nanostructured CZTS thermoelectric material was quite low (0.026 at 700 K) predominantly because of its low electrical conductivity. In contrast, the parent structure of Zn-doped CTS is a ternary p-type

a)E-mail: shinya@jaist.ac.jp. Tel.: +81-(0)761-51-1611

 

semiconductor with a bandgap of 0.9–1.3 eV.[12,13] In the case of Zn-doped CTS, Sn is partly substituted with Zn in the desired amounts.

Pristine zinc blende (ZB) and wurtzite (WZ) $Cu_2SnS_3$ NPs were chemically synthesized as well as Zn-doped $Cu_2Sn_{1-x}Zn_xS_3$ NPs by a heat-up method (for details, see supplementary material). In this study, 6 different types of NPs were synthesized, i.e., ZB $Cu_2SnS_3$, WZ $Cu_2SnS_3$, $Cu_2Sn_{0.95}Zn_{0.05}S_3$, $Cu_2Sn_{0.9}Zn_{0.1}S_3$, $Cu_2Sn_{0.85}Zn_{0.15}S_3$, and $Cu_2Sn_{0.8}Zn_{0.2}S_3$ NPs will be referred to as **Samples A**, **B**, **C**, **D**, **E**, and **F**, respectively, hereafter. Because the as-synthesized NPs were capped with insulating organic ligands [1-dodecanthiol (DDT) and oleylamine (OAM)], it is necessary to remove those ligands from the surface of NPs before making a pellet by PECS. Although the most straightforward way to remove those organic ligands is the thermal treatment of the NPs under inert atmosphere, it leads to the undesirable grain growth of the NPs because high temperature (>450 °C) and long-time treatment is required. Therefore, ligand exchange of the NPs from DDT/OAM to thiourea (TU) was carried out (for details, see supplementary material), because TU sublimates at approximately 170 °C under reduced pressure and thermally decomposes in the temperature range higher than 230 °C.[14] TU-capped **Samples A–F** were then pelletized into solid disks with a diameter of 10 mm and a thickness of 2 – 3 mm by using a PECS machine (Sinterland LABOX-100) under the following conditions: temperature: 450 °C, pressure: 30 MPa, and sintering time: 5 min. Pellets composed of **Samples A–F** will be referred to as **Pellets A–F**, respectively, hereafter. As-synthesized **Samples A–F** were characterized by transmission electron microscopy (TEM, Hitachi H-7650), X-ray diffraction (XRD, Rigaku MiniFlex600 with Cu K$\alpha$), and inductively coupled plasma optical emission spectroscopy (ICP-OES, Shimadzu ICPS-7000). **Pellets A–F** were characterized by XRD, ICP-OES and a scanning TEM (STEM) equipped with a high-angle annular dark-field (HAADF) detector, and energy-dispersive X-ray spectroscopy (EDS) elemental mapping. STEM-HAADF imaging and EDS elemental mapping were performed on a JEOL JEM-ARM200F microscope operated at 200 kV with a spherical aberration corrector and a nominal resolution of 0.8 Å. The specimens for the cross-sectional STEM analyses were prepared by a focused-ion beam (FIB) method.

Figure 1 shows TEM images of as-synthesized **Samples A–F**. All samples are relatively uniform in size and shape except for **Sample A**. Interestingly, **Samples B–F** have a hexagonal pencil-like morphology. By analyzing the TEM images, it was found that **Samples B–F** all have nearly the same size. The average length and width of the NPs were calculated to be 40 and 25 nm, respectively. The Cu:Sn:Zn atomic ratios of as-synthesized **Samples A–F** were determined to be 68:32:0, 69:31:0, 67:31:2, 65:31:4, 63:31:6, and 63:29:8, respectively. The values of $x$ were calculated to be 0, 0, 0.06, 0.11, 0.16, and 0.21 for **Samples A–F**, respectively, which correspond to the input molar ratio of Zn to Sn precursors. This result indicates that Zn was doped stoichiometrically to $Cu_2SnS_3$ substituting Sn presumably because of its similar ionic radius to those of $Sn^{4+}$ (55 pm, C.N. = 4) and $Cu^{+}$ (60 pm, C.N. = 4).[7,15]

Figure 2 shows XRD patterns of **Samples A–F** [Fig. 2(a)] and **Pellets A–F** [Fig. 2(b)]. As shown in Fig. 2(a), the primary crystal phase of **Sample A** is ZB with small amounts of WZ phase (the reference XRD patterns of WZ and ZB CTS were taken from Ref. 16), while the primary crystal phase of **Samples B–F** is WZ with small amounts of ZB phase. As shown in Fig. 2(b), the phase transition from WZ to ZB is clearly seen for **Pellets B–F**. Specifically, **Pellets E** and **F** have a phase-pure ZB crystal structure, while **Pellets B–D** contain small amounts of residual WZ phase. The reason why only **Pellets E** and **F** could obtain a phase-pure ZB structure is possibly because the phase transition temperature decreased by increasing the Zn impurity concentration.

The mean crystalline sizes ($D_{xrd}$) of **Samples A–F** and **Pellets A–F** were estimated using Scherrer's equation for the most intense diffraction peak of the primary phase. As a result, the values of $D_{xrd}$ for **Samples A–F** were calculated to be 24.5, 18.3, 16.9, 20.0, 19.6, and 18.3 nm, respectively.

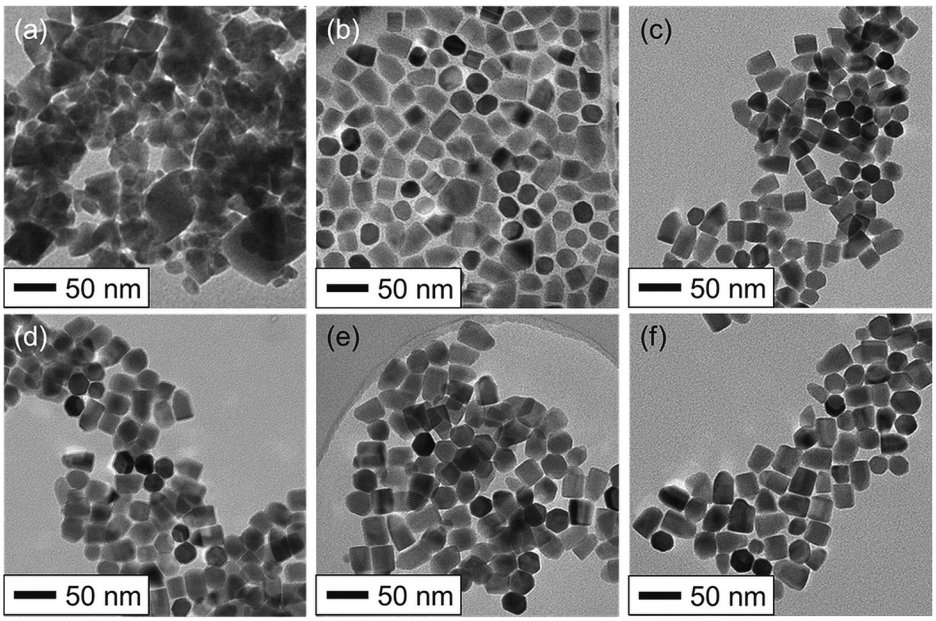


FIG. 1. TEM images of CTS (a) and (b) and Zn-doped CTS (c)–(f) NPs: (a) **Sample A** (ZB), (b) **Sample B** (WZ), (c) **Sample C** ($x = 0.05$), (d) **Sample D** ($x = 0.1$), (e) **Sample E** ($x = 0.15$), and (f) **Sample F** ($x = 0.2$).

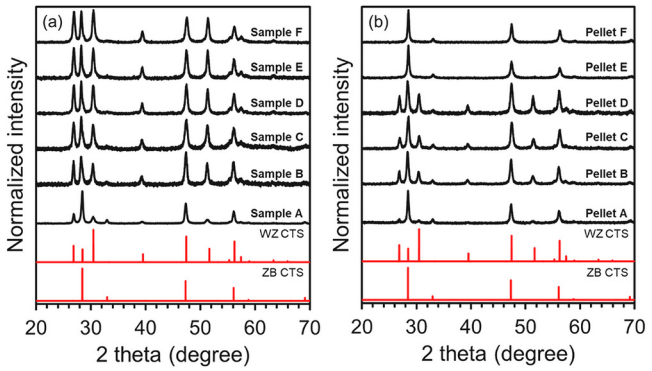


FIG. 2. XRD patterns of (a) **Samples A–F** and (b) **Pellets A–F**. The reference XRD patterns of WZ and ZB CTS[16] are also shown for comparison.

On the other hand, the values of $D_{xrd}$ for **Pellets A–F** were calculated to be 26.8, 21.4, 19.0, 18.2, 24.5, and 27.6 nm, respectively, indicating that the mean crystalline size remains virtually unchanged during sintering for all pellets. The reason why the mean crystalline size of **Sample D** decreased after the sintering is due to the broadening of the primary peak of the ZB phase caused by the non-negligible amount of WZ residue. The compositions of **Pellets A–F** were also found to remain unchanged from those of **Samples A–F**. The densities of **Pellets A–F** were determined to be 4.45, 4.43, 4.57, 4.56, 4.50, and 4.48 g/cm$^3$, respectively, using a gas pycnometer (Shimadzu AccuPyc II 1340). Because the density of monocrystalline ZB CTS is 4.73 g/cm$^3$, the relative densities of **Pellets A–F** were calculated to be $94-97\%$. The cross-sectional STEM-HAADF and EDS elemental mapping images of **Pellets B** and **D** are shown in Fig. S1 in the supplementary material. The contrast of the STEM-HAADF image is relatively uniform in both cases even though some dark areas were observed suggesting the successful formation of homogeneous pellets. The EDS elemental mapping images also confirm that the pellets are compositionally uniform.

Finally, thermoelectric measurements were performed for **Pellets A–F**. First, thermal conductivity ($\kappa$) was measured for the pellet in the cross-plane direction by laser flash analysis (Netzsch LFA457). In this method, $\kappa$ (W·m$^{-1}$·K$^{-1}$) was calculated as $\kappa = dcD$, where $d$ (kg·m$^{-3}$), $c$ (J·kg$^{-1}$·K$^{-1}$), and $D$ (m$^2$·s$^{-1}$) are the density, specific heat, and thermal diffusivity of the pellet, respectively. The values of $c$ and $D$ for **Pellets A–F** are shown in Fig. S2 in the supplementary material. Then, Seebeck coefficient ($S$) and electrical resistivity ($\rho$) were measured in the in-plane direction. The details of measurements are also described in the supplementary material. Carrier thermal conductivity ($\kappa_{carrier}$) was calculated by Wiedemann-Franz's law $\kappa_{carrier} = L\sigma T$, where $L$ and $\sigma$ denote the Lorenz number ($2.44 \times 10^{-8}$ W·Ω·K$^{-2}$) and the electrical conductivity, respectively. Then, lattice thermal conductivity ($\kappa_{lattice}$) was calculated as $\kappa_{lattice} = \kappa - \kappa_{carrier}$. The power factor ($PF$) and $ZT$ value were calculated as $PF = \sigma S^2$ and $ZT = \sigma S^2 T/\kappa$, respectively. Figure 3 shows the temperature dependence of $\sigma$, $S$, $\kappa$, $\kappa_{lattice}$, $PF$, and $ZT$ for **Pellets A–F**. The $ZT$ values of **Pellets A–F** with error bars are shown in Fig. S3 in the supplementary material. It should be noted that we measured $S$ and $\sigma$ in both heating and cooling cycles and found that the values coincide in both cycles (Figs. S4 and S5 in the supplementary material). Therefore, the values only in the heating cycle are shown here. For comparison, the data of undoped non-nanostructured CTS taken from Ref. 7 are shown in Fig. 3.

As seen in Figs. 3(a), 3(b), and 3(e), **Pellet B** showed similar values of $\sigma$, $S$, and $PF$ to non-nanostructured CTS, while it had lower $\kappa$ and $\kappa_{lattice}$ values than non-nanostructured CTS [Fig. 3(c)]. This suggests that the phonon scattering is successfully facilitated with maintaining good carrier transport properties by nanostructuring. It is more evident in the inset of Fig. 3(d), where $\kappa_{lattice}$ of non-nanostructured CTS exhibits the classical $1/T$ dependence caused by Umklapp scattering, while the characteristic $1/T$ dependence of $\kappa_{lattice}$ completely disappears in the case of **Pellet B** supporting the fact that the phonon scattering is dominated by defect scattering. In the case of non-nanostructured CTS, it has been reported that a chemically ordered monoclinic phase has larger $\kappa_{lattice}$ than the chemically disordered cubic/tetragonal phase.[7] This might be because the random distribution of metal atoms and vacancies plays an important role in suppressing $\kappa_{lattice}$ possibly by thoroughly disrupting the normal phonon transport. In the present case, **Pellets A**, **E**, and **F** (ZB CTS without the WZ phase) exhibited higher $\kappa_{lattice}$ than **Pellets B–D** (ZB CTS with the WZ phase). This is presumably because the coexistence of ZB and WZ phases is responsible for the phonon scattering at the interfaces and grain boundaries.

As shown in Fig. 3(b), the sign of $S$ is positive in all cases, confirming p-type carrier transport. With the increasing Zn concentration, $x$, in the Zn-doped CTS (**Pellets C–F**), a systematic increase in $\sigma$ was observed [Fig. 3(a)], while $S$ decreased in an opposite manner [Fig. 3(b)]. In addition, $\sigma$ of **Pellet B** increases with increasing temperature showing a semiconductor behavior, while $\sigma$ of **Pellets C–F** remains unchanged or decreases with increasing temperature showing a metallic behavior. To clarify the effect of Zn-doping on the electronic structure of CTS, the density of states (DOS) of undoped CTS (ZB-phase $Cu_2SnS_3$) and Zn-doped CTS (ZB-phase $Cu_2Sn_{0.9375}Zn_{0.0625}S_3$) was determined using first-principles calculations based on density functional theory (DFT) within the generalized gradient approximation (GGA) in the scheme of Perdew-Burke-Ernzerhof (PBE) functional with the consideration of spin-orbit coupling (SOC) as shown in Fig. S6 in the supplementary material. In consequence, it has been found that the chemical potential ($\mu$) decreases by substituting Sn with Zn leading to hole doping. As a result, $\sigma$ increases while $S$ decreases (for details, see Fig. S7 in the supplementary material).

Interestingly, however, a sharp increase in $\sigma$ is clearly observed when $x$ is increased from 0.1 (**Pellet D**) to 0.15 (**Pellet E**) as shown in Fig. 3(a). This suggests that the electronic transport properties of Zn-doped CTS are influenced not only by the Zn concentration but also by the crystalline structure. As discussed earlier, **Pellets E** and **F** have a phase-pure ZB crystal structure, while **Pellets B–D** contain small amounts of residual WZ phase [Fig. 2(b)]. In general, the ZB compound is expected to have smaller effective masses, higher carrier mobility, and higher doping efficiency than its WZ counterpart, because of its highly symmetric cubic

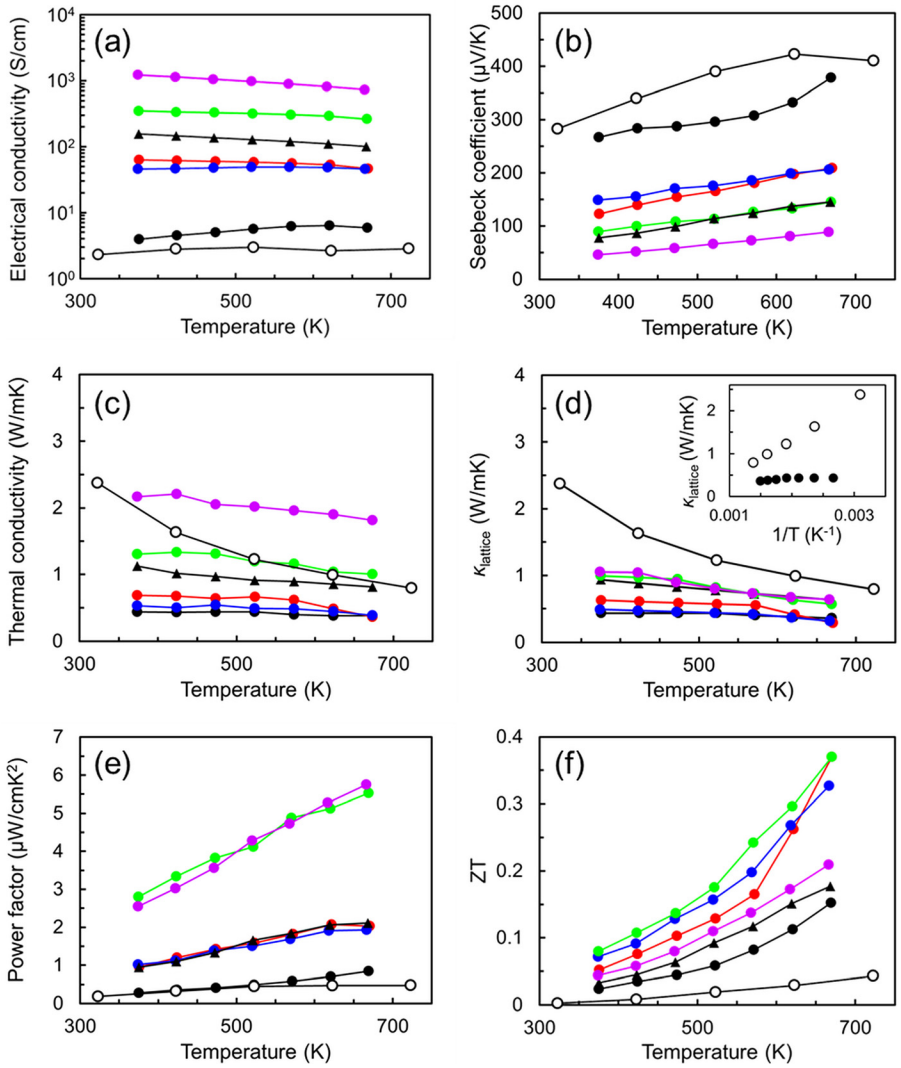


FIG. 3. (a) Electrical conductivity $\sigma$, (b) Seebeck coefficient $S$, (c) thermal conductivity $\kappa$, (d) lattice thermal conductivity $\kappa_{lattice}$, (e) power factor $PF$, and (f) $ZT$ of **Pellets A–F**. Filled black triangles, filled black circles, filled red circles, filled blue circles, filled green circles, and filled purple circles represent **Pellets A–F**, respectively. The open circle represents the data of undoped non-nanostructured monoclinic CTS taken from Ref. 7. The inset of (d) shows $\kappa_{lattice}$ of **Pellet B** (filled black circles) and undoped non-nanostructured CTS (open circles) plotted with respect to the reciprocal of temperature. It should be noted that we measured $S$ and $\sigma$ in both heating and cooling cycles and found that the values coincide in both cycles. Therefore, the values only in the heating cycle are shown here.

structure.[17] Therefore, the presence of the WZ phase in the pellet might create an adverse effect on $\sigma$. To confirm this hypothesis, the values $\sigma$ of **Pellets A** (ZB CTS without the WZ phase) and **B** (ZB CTS with the WZ phase) were compared. As shown in Fig. 3(a), **Pellet A** showed a metallic behavior with higher $\sigma$, while **Pellet B** exhibited a semiconductor behavior with significantly low $\sigma$. This result clearly validates the hypothesis. Unfortunately, it is unclear which is the main contributing factor for lowering of $\sigma$—the existence of interfaces between ZB (high $\sigma$) and WZ (low $\sigma$) phases or the existence of the WZ phase (low $\sigma$) itself, because it was difficult to fabricate a pellet which has a phase-pure WZ structure.

As shown in Fig. 3(f), the $ZT$ values monotonically increase with temperature in all pellets and the highest $ZT$ value of 0.37 at 670 K is achieved in both **Pellets C** ($Cu_2Sn_{0.95}Zn_{0.05}S_3$) and **E** ($Cu_2Sn_{0.85}Zn_{0.15}S_3$). In the case of non-nanostructured $Cu_2Sn_{1-x}Zn_xS_3$, the highest $ZT$ value is reported to be 0.58 in the $x = 0.10$ sample at 723 K.[7] In this study, we set an upper temperature limit of 670 K for the thermoelectric property measurements to ensure that the pellets will not be chemically altered. Thus, if we compare the $ZT$ values of **Pellet C** or **E** and non-nanostructured $Cu_2Sn_{1-x}Zn_xS_3$ ($x = 0.10$) at the same temperature, they are comparable.

In conclusion, the CTS system contains environmentally benign and abundant elements and exhibits modest thermoelectric properties at relatively low temperature range. In theory, introducing nanograins into a CTS-based thermoelectric material in a controlled manner enables us to enhance its $ZT$ value in comparison to the non-nanostructured counterpart by reducing $\kappa_{lattice}$ while maintaining $PF$. In addition, further enhancement of the $ZT$ value can be achieved through doping of another element such as Zn in these materials. In this study, both strategies are employed to improve the $ZT$ value of CTS-based sustainable thermoelectric materials. In particular, the chemically synthesized $Cu_2Sn_{1-x}Zn_xS_3$ ($x = 0 - 0.2$) NPs were pelletized by a pulse electric current sintering method. The highest $ZT$ value of 0.37 at 670 K is achieved in both $Cu_2Sn_{0.95}Zn_{0.05}S_3$ and $Cu_2Sn_{0.85}Zn_{0.15}S_3$ nanostructured materials. However, this value was comparable to the $ZT$ value at the same temperature of the $Cu_2Sn_{0.9}Zn_{0.1}S_3$ non-nanostructured material[7] presumably because the advantages and disadvantages of nanostructuring are balanced out in this case. Our ongoing work has focused on the further improvement of the $ZT$ value by optimizing the size and shape of the NPs, blending two or more different types of NPs [e.g., ZB-phase Zn-doped CTS and mixed-phase (ZB + WZ) Zn-doped CTS] for making a bulk material, and controlling mesoscale structures by tuning sintering conditions.

See supplementary material for the synthesis scheme of nanoparticles, the ligand exchange protocol, the cross-sectional STEM-HAADF and EDS elemental mapping images, the details of thermoelectric property measurements, the values of $c$, $D$ and $ZT$ for **Pellets A–F**, the values of $S$ and $\sigma$ measured both in heating and cooling cycles, and DOS of undoped and Zn-doped CTS.

This work was supported by NEDO Research and Development for Innovative Use of Unused Thermal Energy and the Mazda Foundation Research Grant. This work at AIST was supported as part of the International Joint Research Program for Innovative Energy Technology funded by the Ministry of Economy, Trade and Industry (METI), Japan. The authors thank Ms. Naoko Fujimoto of AIST for operating the ZEM-3 and LFA457 and Mr. Atsushi Yamamoto of AIST for supporting these measurements. The authors also thank Koichi Higashimine of JAIST for help with STEM measurements.

[1]Z.-H. Ge, B.-P. Zhang, Y.-X. Chen, Z.-X. Yu, Y. Liu, and J.-F. Li, Chem. Commun. **47**, 12697 (2011).
[2]K. Suekuni, K. Tsuruta, M. Kunii, H. Nishiate, E. Nishibori, S. Maki, M. Ohta, A. Yamamoto, and M. Koyano, J. Appl. Phys. **113**, 043712 (2013).
[3]K. Suekuni, F. S. Kim, H. Nishiate, M. Ohta, H. I. Tanaka, and T. Takabatake, Appl. Phys. Lett. **105**, 132107 (2014).
[4]J. Heo, G. Laurita, S. Muir, M. A. Subramanian, and D. A. Keszler, Chem. Mater. **26**, 2047 (2014).
[5]X. Lu, D. T. Morelli, Y. Xia, and V. Ozolins, Chem. Mater. **27**, 408 (2015).
[6]Y. Bouyrie, M. Ohta, K. Suekuni, Y. Kikuchi, P. Jood, A. Yamamoto, and T. Takabatake, J. Mater. Chem. C **5**, 4174 (2017).
[7]Y. Shen, C. Li, R. Huang, R. Tian, Y. Ye, L. Pan, K. Koumoto, R. Zhang, C. Wan, and Y. Wang, Sci. Rep. **6**, 32501 (2016).
[8]Q. Tan, W. Sun, Z. Li, and J.-F. Li, J. Alloys Compd. **672**, 558 (2016).
[9]H. Zhao, X. Xu, C. Li, R. Zhang, R. Huang, Y. Lv, D. Li, X. Hu, L. Pan, and Y. Wang, J. Mater. Chem. A **5**, 23267 (2017).
[10]K. Biswas, J. He, I. D. Blum, C.-I. Wu, T. P. Hogan, D. N. Seidman, V. P. Dravid, and M. G. Kanatzidis, Nature **489**, 414 (2012).
[11]H. Yang, L. A. Jauregui, G. Zhang, Y. P. Chen, and Y. Wu, Nano Lett. **12**, 540 (2012).
[12]P. A. Fernandes, P. M. P. Salomé, and A. F. da Cunha, J. Phys. D: Appl. Phys. **43**, 215403 (2010).
[13]Y.-T. Zhai, S. Chen, J.-H. Yang, H.-J. Xiang, X.-G. Gong, A. Walsh, J. Kang, and S.-H. Wei, Phys. Rev. B **84**, 075213 (2011).
[14]S. Wang, Q. Gao, and J. Wang, J. Phys. Chem. B **109**, 17281 (2005).
[15]R. D. Shannon, Acta Crystallogr., Sect. A: Cryst. Phys., Diffr., Theor. Gen. Crystallogr. **32**, 751 (1976).
[16]Q. Liang, Eur. J. Inorg. Chem. **2016**, 3634 (2016).
[17]G. M. Dalpian and S.-H. Wei, Phys. Rev. Lett. **93**, 216401 (2004).